Acoustic intensity based data analysis and assessment in computational aeroacoustics

Christoph Richter [a],*, Klaus Ehrenfried [b], Norbert Schönwald [a], Mathias Steger [a], Frank Thiele [a]

[a] Institute of Fluid Mechanics and Engineering Acoustics, Technische Universität Berlin, Sekr. MB1, Strasse des 17. Juni 135, Berlin 10623, Germany
[b] Institute of Aerodynamics and Flow Technology, German Aerospace Center, Bunsenstr. 10, Göttingen 37073, Germany

ARTICLE INFO

ABSTRACT

A methodology for assessing the quality and analysing the sound field of a numerical solution for an aeroacoustic problem is presented using an in-duct propagation problem as example. Namely an analysis of the acoustic energy conservation provides insight about the solution quality; sources of numerical error as well as physical source of sound are located by an analysis of the acoustic intensity; a mode analysis provides information about the sound field in the duct and a visualisation of the average pathway of sound by the acoustic intensity helps the interpretation of the modal amplitude data. The problem chosen for the presentation deals with the propagation of a single acoustic mode upstream through the tapering inlet duct of a centrifugal compressor. The propagation of tone noise is a typical problem for computational aeroacoustics. The numerical approach employs high-order finite-difference discretisation schemes with structured body-fitted meshes. An overset grid approach allows to overcome the geometrical complexity of the problem. The conservation of the acoustic energy is found to be violated by less than 3% in case of a potential base flow. In this case major sources of error are found in the interpolation between overset and background mesh. In case of a non-potential flow with boundary layers at the wall, the conservation of acoustic energy cannot be claimed. Consequently, it shows an increase of the acoustic energy, for which the accelerated flow in the nozzle is identified as source. It is shown that the filtering scheme affect the solution more than the spatial discretisation, if the grid resolution is relatively high. A strong scattering of energy into higher radial modes is detected. The fifth and sixth radial mode are found to be preferred in the current example. They are excited in the nozzle with a similar level. For these high radial modes, the transport of acoustic energy takes place further away from the duct wall. This explains the relatively large drop of about 20 dB for the average sound pressure level at the wall over the inlet nozzle.

1. Introduction

The prediction and understanding of the in-duct propagation of turbo-machinery noise is one of the major objectives for the development of numerical methods in computational aeroacoustics (CAA). Different from the low-order methods, which are classically used in computational fluid dynamics (CFD) to obtain the steady flow physics, CAA methods are using high-order approximations. Therefore, they have the potential to describe acoustic propagation and help in developing quiet turbo-machinery from the drawing board. Especially for tonal noise and modal propagation, which play a major role

---

* Corresponding author. Tel.: +49 30 314 24733; fax: +49 30 314 25405.
E-mail address: Christoph.Richter@TU-Berlin.de (C. Richter).

Nomenclature		$\mathbf{x}$	position vector in physical domain
		x	coordinates in physical domain
c	speed of sound		
C_{ij}	interpolation coefficient		
$\mathbf{e}$	Cartesian unit vector		
e_a	acoustic energy per unit volume	ϕ	state of the fluid
i	index of spatial discretisation and imaginary unit	ϱ	density
		σ	directional damping coefficient
$\mathbf{I}$	acoustic intensity	ξ	coordinate in computational domain
j	index of spatial discretisation	η	coordinate in computational domain
L	Lagrange polynomial		
m	azimuthal mode number		
$\mathbf{n}$	surface normal		
n	radial mode number	$'$	small perturbation
p	pressure	$*$	interpolated
P	acoustic power		
QPL	source power level		
q	acoustic source		
S	surface		
$\mathbf{u}$	velocity vector	0	mean flow state
u	axial velocity component	φ	azimuthal component
v	radial velocity component	r	radial component
w	azimuthal velocity component	x	axial component

in the inlet section of turbines and compressors, many successful applications are reported. In this context CAA is able to predict mode scattering and mean flow effects as well as the influence of complex geometries on the sound propagation. Current CAA methods use optimised high-order discretisation schemes together with perturbation approaches, which theoretically allow an exploration of the sound field down to the threshold of audibility with a minimal number of grid points.

However, such applications require a reliable stability and provable accuracy of the computational method. These requirements are often conflicting goals for CAA methods, which use artificial dissipation and dissipative filtering to obtain stable solutions for a non-dissipative physical problem. Even though this is not necessary, CAA methods are usually applied with a non-conservative mathematical model solving a perturbation equation about an arbitrary base flow. No conservation laws apply in general for the acoustic perturbation [1]. Thus, the application of non-conservative finite-difference schemes as the Dispersion-Relation-Preserving scheme of Tam DRP [7] for CAA method seems legitimate. However, it opens the door for speculations about the accuracy of the numerical result. Therefore, a general method to prove the accuracy of such solutions seems a necessary condition for the acceptance of CAA methods.

The problem cannot simply be overcome by going back to the classical CFD methods. Even though, these methods are conservative, their properties with respect to the propagation of acoustic waves are far from the desired accuracy and resolution limits. Furthermore, the major advantages of the CAA methods as integral part of a physical domain decomposition are based on the specific mathematical perturbation approach about an average flow field and the numerical high-order modelling. In addition, for an efficient application of CAA, the modelled problem has to clip the reality, which introduces modelling errors at the same time. Such errors can result from the application of a simplified model equation and the reduction of the model dimensions. In addition, a discrete sampling of space and time functions is performed, which produces cut-off errors. Moreover, commonly used techniques as selective damping or digital filtering of the solution add dissipation to the result, which should not affect the resolved range of wavenumbers. For many of the high-order CAA methods, these techniques are required to ensure the stability of the method. As will be shown, it is easy to get 20 dB off the exact solution by applying a slightly more dissipative filter. Therefore, a proof of the numerical solution for artificial dissipation seems highly recommended. Another important error source is the structured meshing of complex geometries, which often leads to stretched and skewed grids in the physical domain. These are then mapped to an orthogonal mesh in the computational domain and the mapping spreads the wavenumber spectrum. In consequence parts of the solution are mapped into the unresolved range of wavenumbers. Thus, such meshes for complex geometries are known to increase numerical errors, as grid oscillations and dissipation. A possible way to overcome the problem is the application of an overset grid technique, with a high-order interpolation between body-fitted and background mesh. However, numerical dissipation due to the interpolation error is unavoidable for this solution and should be quantified. Finally, the introduction of artificial non-reflective boundary conditions can lead to errors.

The analysis of the acoustic intensity, as it is proposed in the current paper, could remove the uncertainty. Even though there is no way to find a general conservation law for the acoustic energy, the analysis would allow to assess the quality of the solution and locate physical sound sources together with non-physical error sources in a numerical solution. The current paper uses the acoustic energy and intensity defined by Morfey [1] for this purpose.
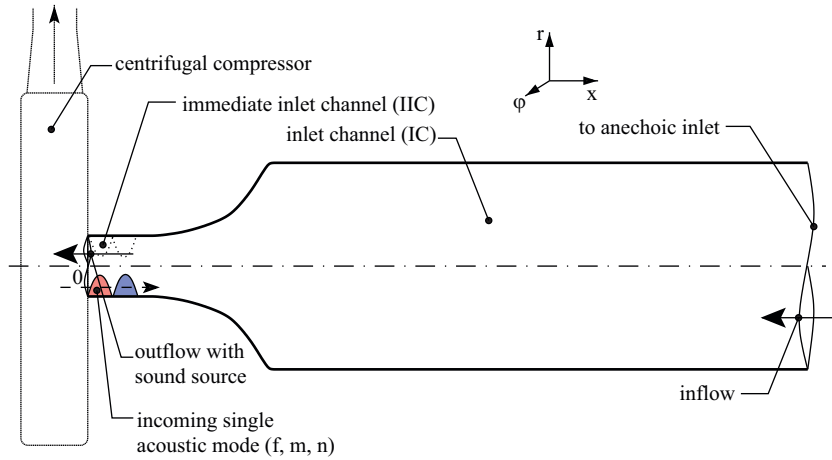
Fig. 1. Sketch of the inlet duct considered as test case.

The centrifugal compressor inlet duct shown in Fig. 1, which is experimentally investigated by the German Aerospace Center (DLR) [3] is chosen as an example problem. Different from the usual convention, the flow direction is from the right to the left in all figures throughout the paper, whereas the acoustic waves propagate conventionally from the left to the right. The compressor radiates harmonics of the blade passing frequency as tones in high azimuthal modes into the narrow immediate inlet channel (IIC, see Fig. 1). These modes then propagate upstream against the flow at $Ma = 0.3$ through the inlet nozzle with decreasing flow velocity. Finally, they travel upstream the wider inlet channel (IC in Fig. 1) into an anechoic termination. The inlet nozzle couples the narrow IIC to a wider inlet channel (IC) upstream. Due to the different diameter and almost independent of the azimuthal mode number, 10 radial modes are cut-on in the IC when only one radial mode of the same azimuthal mode can propagate in the IIC. Measurements for the problem have been carried out by Raitor et al. with a rotating microphone array [3].

The current numerical investigation was motivated by the observation of a large decrease of the sound pressure level of nearly all higher azimuthal modes at various frequencies, when considering measurement positions in the narrow (IIC) and in the wide inlet duct (IC) of the centrifugal compressor sketched in Fig. 1. This observation cannot be explained by simple models like an equal distribution of power over the duct area or the assumption of the acoustic energy remaining in the same mode. Both assumptions would explain only about 10 dB decrease of the sound pressure level at the wall for the about 10 times larger area of the IC with respect to the IIC. The observed average decrease is typically in the range of 20 dB for all modes and tones, when considering a spatial average of the sound pressure level along the wall. However, due to the tapering inlet nozzle mode scattering occurs and the acoustic field becomes relatively complex. Thus, an assessment of the numerical solution by considering the pressure amplitude or sound pressure level becomes impossible and an analysis of the acoustic intensity is an useful approach to verify the solution.

The centrifugal compressor inlet duct problem features all typical properties for in-duct CAA applications as there are the presence of higher azimuthal modes at high frequencies in a varying mean flow and a varying duct area. Moreover, the open area of the inlet duct changes by the factor of 10, which makes the geometry complex in the sense of a CAA method designed for structured Cartesian meshes. This problem is overcome by an overset grid approach here. Furthermore, the whole problem is axisymmetric, thus a modal axisymmetric mathematical model is used and the computation is carried out in two dimensions.

The paper is organised as follows: In Section 2 mathematical models and numerical methods are briefly presented. The intensity definition used throughout the paper to access the solution is given in Section 3. The test case, mean flow and grid details are presented in Section 4. A detailed analysis of intensity and modal content is given together with the results in Section 5. Different model equations and mean flow assumptions are compared and analysed. Finally, conclusions are drawn in Section 6.

2. Mathematical model and numerical method

2.1. Mathematical models

The governing equations describing the propagation of all linear perturbations in an arbitrary moving fluid are the linearised Euler equations (LEE):

$$\frac{\mathrm{D}\varrho'}{\mathrm{D}t} + \mathbf{u}' \cdot \boldsymbol{\nabla}\varrho_0 + \varrho_0\boldsymbol{\nabla} \cdot \mathbf{u}' + \varrho'\boldsymbol{\nabla} \cdot \mathbf{u}_0 = 0, \tag{1a}$$

$$\frac{D\mathbf{u}'}{Dt} + \frac{\varrho'}{\varrho_0}\mathbf{u}_0 \cdot \nabla\mathbf{u}_0 + \mathbf{u}' \cdot \nabla\mathbf{u}_0 + \frac{1}{\varrho_0}\nabla p' = 0, \tag{1b}$$

$$\frac{Dp'}{Dt} + \gamma p_0 \nabla \cdot \mathbf{u}' + \mathbf{u}' \cdot \nabla p_0 + \gamma p' \nabla \cdot \mathbf{u}_0 = 0. \tag{1c}$$

The material derivative $D \cdot /Dt$ is given by

$$\frac{D\cdot}{Dt} = \frac{\partial\cdot}{\partial t} + \mathbf{u}_0 \cdot \nabla(\cdot),$$

where the transport velocity is given by the average flow speed $\mathbf{u}_0$.

For isentropic mean flow conditions and perturbation, the energy equation for the pressure (Eq. (1c)) can be replaced by the algebraic relation:

$$p' = c^2\varrho', \tag{1d}$$

with the square of the speed of sound defined as follows:

$$c^2 = \gamma\frac{p_0}{\varrho_0}.$$

The duct geometry and mean flow conditions are considered axisymmetric. A harmonic approach is introduced for the azimuthal variation of the perturbations assuming an axisymmetric base flow field as given by Li et al. [4]. Then, the gradient is defined as follows for the mth azimuthal Fourier component:

$$\nabla_{\text{Axi}} = \frac{\partial}{\partial x}\mathbf{e}_x + \frac{\partial}{\partial r}\mathbf{e}_r + \frac{im}{r}\mathbf{e}_\varphi.$$

For the cylindrical coordinate system, the derivatives of the basis vectors $\mathbf{e}_r$ and $\mathbf{e}_\varphi$ have to be considered in addition. The three-dimensional solution is obtained as the superposition of an infinite number of azimuthal Fourier components in general. However, in many cases the number of azimuthal modes m is limited due to the specific sound source or geometry considered, which leads to an advantage of the current modal axisymmetric approach over the full three-dimensional computation. The system is written in matrix–vector-form as

$$\frac{\partial\boldsymbol{\phi}'}{\partial t} = -\mathbf{A} \cdot \frac{\partial\boldsymbol{\phi}'}{\partial x} - \mathbf{B} \cdot \frac{\partial\boldsymbol{\phi}'}{\partial r} - \frac{1}{r}\mathbf{C} \cdot \boldsymbol{\phi}' - \mathbf{D} \cdot \boldsymbol{\phi}', \tag{2}$$

with $\boldsymbol{\phi}'$ as the vector of perturbation quantities. The matrices $\mathbf{A}$, $\mathbf{B}$, $\mathbf{C}$ and $\mathbf{D}$ contain the coefficients obtained from Eq. (1) for the LEE. In addition to these linear modal axisymmetric models, a system of perturbed nonlinear non-conservative Euler equations (PENNE [5]) is available for fully axisymmetric problems [6], which is employed here to calculate the average mean flow field for the perturbation approach.

2.2. Discretisation schemes

The numerical method is based on the fourth-order Dispersion-Relation-Preserving (DRP) scheme [7] for the spatial discretisation. At the boundaries such as the walls and the open ends of a duct, optimised backward stencils of fourth-order are used. The time integration is performed by the alternating five/six stage Low-Dissipation–low-dispersion-Runge–Kutta (LDDRK) method [8] implemented in 2N storage form [9].

2.2.1. Filtering of the solution

According to Tam et al. [10] all high-order finite-differencing schemes are affected by spurious grid oscillations, which are related to not fully resolved short-wave components in the solution. A central, seven-point-stencil, standard filter (FIR) of sixth order is applied at every 10th full Runge–Kutta step in order to eliminate parasite waves [6]. The filter is defined as the approximation ϕ^* of a field variable ϕ at the point l which is based on the neighbouring points $l - N$ to $l + N$ as

$$\phi_l^* = \phi_l - \sigma_{\text{filter}} \sum_{j=-N}^{N} w_j\phi_{l+j}, \tag{3}$$

where the filter coefficient σ_{filter}, $0 < \sigma_{\text{filter}} < 1$, controls the effect of the filter. A full filtering is achieved by $\sigma_{\text{filter}} = 1$, whereas the attenuation of waves in the transition zone of the seven-point-stencil filter is reduced by specifying $\sigma_{\text{filter}} = 0.2$. The filter coefficients for the low-pass filter are obtained from a Taylor series expansion equation (3) setting $\sigma_{\text{filter}} = 1$. For $\sigma_{\text{filter}} = 1$, the transfer function of the filter in the wavenumber space is given by the response to a spatially harmonic excitation with the relative wavenumber $k\Delta x$ as

$$\Psi = 1 - \sum_{j=-N}^{N} w_j e^{ijk\Delta x}. \tag{4}$$

At domain boundaries, the seven-point-stencil central filter cannot be applied. It is found that a filtering with shorter filter stencils has a favourable effect on the stability, when applied towards the wall ($N = 3 \ldots 0$). However, to avoid too high dissipation due to these short filters, the filter coefficient σ_{filter} is reduced with decreasing filter order according to the empirical law

$$\sigma_{\text{filter}}^{(N)} = \left(\frac{2N+1}{11}\right)^2 \sigma_{\text{filter}}^{N=5}.$$ (5)

2.3. Meshing variations of the geometry by overset grids

The application of a finite-difference CAA method that employs high-order discretisation schemes necessitates a structured mesh. For a complex geometry, block-structured, curvilinear, body-fitted grids have to be used, which causes two major difficulties. On the one hand it is tedious and challenging to generate a good quality mesh with less distorted cells to avoid numerical errors. On the other hand large overlapping areas at the block boundaries cause grid singularities on intersections of odd number of block joints. To avoid these two problems, speed up the grid generation process and increase the overall grid quality, the presented CAA solver uses an overset grid approach [11].

An orthogonal and equidistant host grid spans the whole computational domain. The solids in the domain are separately meshed with high quality body-fitted grids. These grids are set over the host grid. The data transfer between the individual overset grids and the host grid is accomplished by a high-order interpolation method, using a Lagrange polynomial approach.

Applying a 4×4-point stencil (see Fig. 2), the node coordinates in the destination grid $\mathbf{x}^*$ can be written in terms of the node coordinates in the source grid $\mathbf{x}$ by

$$\mathbf{x}^* = \mathbf{x}(\xi, \eta) = \sum_{i=0}^{3} \sum_{j=0}^{3} \mathbf{x}_{i_0+i, j_0+j} C_{ij}(\xi, \eta).$$ (6a)

The interpolation coefficients C_{ij} yield to

$$C_{ij}(\xi, \eta) = L_i(\xi) L_j(\eta),$$ (6b)

by using of Lagrange polynomials

$$L_i(\xi) = \prod_{n=0; n \neq i}^{3} \frac{\xi - n}{i - n}$$ (6c)

and can be calculated by solving the nonlinear equation (6a).

A tool used for searching the origins $\mathbf{x}_{i_0 j_0}$ of the interpolation stencils and for the identification of areas excluded from solving in the host grid was developed and is used in the preprocessing [11]. Therefore, the overhead in each time step due to the overset grid technique is minimised. During the simulation, only the perturbation quantities $\phi' = (\varrho', u', v', w', p')^T$ have to be interpolated by Eq. (7), using the predefined coefficients C_{ij}:

$$\phi'^* = \phi'(\xi, \eta) = \sum_{i=0}^{3} \sum_{j=0}^{3} \phi'_{i_0+i, j_0+j} C_{ij}(\xi, \eta).$$ (7)
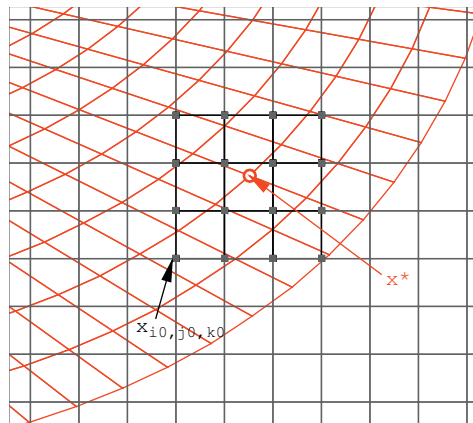

Fig. 2. Stencil used for interpolation from the source grid (straight) to the overset grid (curved).

As a consequence, the CAA solver retains efficiency, whereas the grid generation is eased dramatically. The overset grid approach increases the grid quality and accuracy of the result significantly.

2.4. Boundary conditions

2.4.1. Non-reflective boundary condition
The non-reflective boundary condition for open duct ends is based on the perfectly matched layer (PML) of Hu [12]. The vector component of the damping σ_x is increased towards the outer boundary at an open end. In addition, the outermost grid line is set zero for all perturbation components. A simple sponge layer that adds damping is used at the boundary with an incoming sound source:

$$\frac{\partial \phi'}{\partial t} = \mathbf{F}(\phi') - \sigma_x(\phi' - \phi'_{\text{source}}).\tag{8}$$

The sound source is defined by ϕ'_{source}, which could be an arbitrary time dependent perturbation in general. Spatially, a single Fourier component is considered in azimuthal direction, while the axial and radial directions are free. At the outermost three grid lines the source is given as a Dirichlet boundary condition.

2.4.2. Modal symmetry condition
A modal symmetry boundary condition with a singularity treatment is used at the axis. It is based on the assumption that the solution for the mode m is a superposition of various radial modes of this azimuthal mode for each frequency. When considering the analytical solution in a straight cylindrical duct without centre body and with plug flow according to [4] these modes are described as Bessel functions of the order m. With r approaching to zero these modes behave as a Bessel function of the first kind of the order m for p', ϱ' and u'. The mth-order Bessel function of the first kind tends to the limit of $p'\varrho'$ and $u' \sim r^m$ with r approaching to zero. The radial and azimuthal velocity components of such modes behaves as the derivative of the mth-order Bessel function, then. This leads to the limit $v', w' \sim r^{m-1}$ for the radius approaching zero. This limit for modes in a straight duct is used as an approximation of the solution close to the axis where the amplitude of the high azimuthal modes is very low.

Assuming j to be the coordinate direction normal to the axis, the pressure at a point with index j close to the axis can be calculated from the pressure perturbation p'_{j+1} further away from the axis as follows:

$$p'_j = \left(\frac{r_j}{r_{j+1}}\right)^m p'_{j+1}.\tag{9}$$

The density and axial velocity follow the same law, but due to the radial derivative for the radial acoustic velocity component and the additional division by r for the azimuthal component, the following interpolation law is applied at the axis:

$$v'_j = \left(\frac{r_j}{r_{j+1}}\right)^{m-1} v'_{j+1}.\tag{10}$$

The above approximation is used in an environment around the axis to avoid a small time step size due to the stiff character of the mathematical model for small r. In the current example the interpolated region covers up to three grid spacings from $r = 0$. In addition, three points below the axis are defined, to keep with the central differencing scheme at the axis. These points are obtained by mirroring the perturbation field from the three points above the axis.

2.4.3. Wall boundary condition
The boundary condition for hard walls is based on the idea of Tam and Dong [13] to introduce a ghost point pressure. However, the ghost point is neither stored nor part of the mesh. The implementation is described in detail by Richter et al. [14].

3. Acoustic intensity analysis

In the present paper the acoustic intensity in the definition of Morfey [1] is used to access the quality of the acoustic solution and compare the different modelling assumptions. Using the acoustic intensity to assess the quality of a numerical solution is not a completely new idea. It has been proposed for instance by Eversman before [15]. However, within a large number of publications considering CAA methods there are only few authors who provide an analysis of the acoustic intensity with their solutions.

3.1. Definition and conservation of the acoustic energy

The usefulness of the concept of acoustic power depends on the validity of a continuity principle for the fluctuation energy. In general the conservation of acoustic energy can be expressed in the form

$$\frac{\partial e_a}{\partial t} + \mathbf{\nabla} \cdot \mathbf{I} = q,\tag{11a}$$

where e_a denotes the acoustic energy per unit volume, $\mathbf{I}$ is the acoustic intensity, and q is the production rate of acoustic energy per unit volume. Following Morfey [1], the definitions

$$e_a = \frac{p'^2}{2\rho_0 c_0^2} + \frac{\rho_0}{2}\mathbf{v'_a} \cdot \mathbf{v'_a} + \rho'\mathbf{u}_0 \cdot \mathbf{v'_a} \tag{11b}$$

and

$$\mathbf{I} = (p' + \rho_0\mathbf{u}_0 \cdot \mathbf{v'_a})\left(\mathbf{v'_a} + \frac{p'}{\rho_0}\mathbf{u}_0\right) \tag{11c}$$

are used here. These definitions can be regarded as a generalisation of the classical expressions for acoustic energy and intensity to non-uniform flow fields. In contrast to the classical situation of a medium at rest or a homogeneous flow, it is not possible to find useful definitions of acoustic energy and intensity for arbitrary inhomogeneous flow fields. In this case, the production rate q on the right-hand side of (11a) is not everywhere found to be zero or at least of third order in fluctuation quantities. However, the definitions (11b) and (11c) have the advantage that q at least vanishes (to second order in fluctuating quantities) in all regions with irrotational flow and uniform specific entropy. Thus, the production of fluctuation energy is limited to regions with non-zero vorticity or entropy variations. There, the quantity q represents the production rate at which acoustic energy is generated in the flow.

3.2. Identification of acoustic sources

Note that q may also be negative, which means that fluctuation energy is annihilated. To obtain the effective production of fluctuation energy one has to consider the temporal average of q. In case of a statistically stationary flow the temporal average of Eq. (11a) yields

$$\mathbf{\nabla} \cdot \langle\mathbf{I}\rangle_t = \langle q\rangle_t, \tag{12}$$

because the mean value of $\partial e_a/\partial t$ vanishes. Hence, the effective production of fluctuation energy can be calculated taking the divergence of the mean acoustic intensity $\langle\mathbf{I}\rangle_t$. This value can be easily calculated from numerical solutions. So Eq. (12) can also be used to assess the quality of computational methods for inhomogeneous flows, where no analytical solution is available for comparison. If the mean flow is a potential flow field, then the production rate of acoustic energy should be negligible. Higher magnitudes of $\langle q\rangle_t$ indicate regions where numerical errors or physical sources lead to generation or annihilation of acoustic energy. Annihilation of acoustic energy occurs, for example when artificial damping of acoustic waves is present due to numerical viscosity or filtering, and an artificial production of fluctuation energy can be caused by numerical instabilities.

3.3. A logarithmic source power level scale for the source strength

The source strength $\langle q\rangle_t$ has an unit of $\mathrm{W\,m}^{-3}$, denoting a specific acoustic power which is input in average from a source with equally distributed additive superposing source strength in a volume of $1\,\mathrm{m}^3$. It shows a large dynamic range. For a better visualisation, a logarithmic scale is chosen which is based on the power spectral density (PSD). The average source strength can be negative, which means an annihilation of acoustic energy. Therefore, the absolute value of the source power is considered to obtain another logarithmic scale for the annihilation of acoustic energy. The resulting two logarithmic scales are put together adding the original sign of $\langle q\rangle_t$ to obtain negative values for sinks and positive ones for sources of acoustic energy. To obtain distinct scales with this properties, sources with an QPL below 0 dB are cut-off by a max operation in the logarithm. Accordingly, the acoustic source power level QPL, which gives the average acoustic power input on a PSD like scale can be defined as

$$\mathrm{QPL} = \mathrm{sgn}(\langle q\rangle_t)10\log_{10}\left[\max\left(\frac{|\langle q\rangle_t|}{10^{-12}\,\mathrm{W\,m}^{-3}}, 1\right)\right]. \tag{13}$$

The QPL becomes zero, if the absolute value of the input source power is below the threshold of $10^{-12}\,\mathrm{W\,m}^{-3}$. The QPL scale is used in the following to visualise the source distribution. The scale is adjusted in order to separate the dominant sources from the background noise.

3.4. Validation of numerical solutions by the conservation of acoustic energy

Beside the analysis, which uses local values of $\langle q\rangle_t$ to asses the quality of a numerical solution, also an integral approach is obvious, where the energy balance over a control volume is considered. The global conservation law is obtained integrating Eq. (12) over a volume V with closed surface S, which leads to

$$\int_S \mathbf{n} \cdot \langle\mathbf{I}\rangle_t \,\mathrm{d}S = \int_V \langle q\rangle_t \,\mathrm{d}V, \tag{14a}$$

where $\mathbf{n}$ is the surface normal, and $\mathbf{n} \cdot \langle \mathbf{I} \rangle_t$ is the (temporal mean) flux density of acoustic energy across the surface S (compare [15]). Relation (14a) is used in the present paper to investigate the conservation of energy in a duct with impermeable side walls. Therefore the mean flux $\langle P \rangle_t$ through a cross section of the duct is considered. This flux can be calculated by

$$\langle P(x) \rangle_t = \int_{S_x} \mathbf{n} \cdot \langle \mathbf{I} \rangle_t \, dS_x, \qquad (14b)$$

where S_x is the area of the respective lateral cut through the duct and $\mathbf{n}$ points in axial direction. The variation of $\langle P \rangle_t$ with axial position x gives an overview about the energy conservation in the duct. Theoretically the flux of acoustic energy through the impermeable side wall is zero. If the duct flow is irrotational and isentropic, then no acoustic energy should be generated or annihilated in the duct, and consequently, because of (14a), the flux $\langle P \rangle_t$ should be identical for all axial positions x. In this case the variation of the average $\langle P \rangle_t$ along x indicates the level at which the global conservation of acoustic energy is violated by a numerical solution.

If the flow is not irrotational or contains entropy variations, which is the realistic scenario for viscous flows, additionally to the numerical errors a natural production of acoustic energy in the flow is possible. Then the numerical disturbance of the acoustic energy balance cannot be easily distinguished from the natural effect. However, it can still make sense to apply the energy analysis in the presence of viscous flows, too. If, for example, changes of numerical parameters have a strong influence on the distribution of $\langle P \rangle_t$ along the duct axis, then there is an indication that the numerical method has problems to describe the balance of acoustic energy in the duct flow correctly.

It has to be noted that the energy analysis in the above form is valid for any acoustic solution in which the fluctuations are statistically stationary. But it is also possible to apply the whole analysis to single transient events, where the fluctuations are zero at the beginning and at the end. In this case the average $\langle \cdot \rangle_t$ is meant over the whole event. In contrast, an application to an initial value problem is not possible, as the change of the acoustic energy in a volume is non-zero in average due to the unsteady initial distribution of the acoustic energy.

4. Test case

4.1. Experimental configuration

The centrifugal compressor inlet configuration introduced before and sketched in Fig. 1 is considered as a test case. The base flow conditions are calculated based on one of the experimentally investigated cases [3]. The exact operation conditions considered here are summarised in Table 1. In the experiment, harmonic tones of the shaft rotation frequency dominate in the configuration at the given operation conditions with a mass flow rate of 2.531 kg/s in the duct [3]. The main tone is radiated in a single $m = 13$, $n = 0$ mode at the blade passing frequency (BPF, 10 896.4 Hz), which is the 13th harmonic of the shaft rotation frequency. This single duct mode is excited in the IIC and the propagation is investigated numerically in order to study the effect of the geometrical boundary conditions and the base flow on the mode scattering in a typical example. However, the large variation in the open area of the duct produces similar conditions for all azimuthal modes cut-on in the IIC and the results may qualitatively apply for other modes at other frequencies too.

4.2. Numerical model

Only the axisymmetric inlet duct with inlet nozzle and immediate inlet duct shown in Fig. 1 are considered in the simulation. The simulation is carried out in the x, r-plane of a cylindrical coordinate system. The azimuthal direction is modelled by the model axisymmetric approach of Eq. (2). The inflow and outflow ends are considered anechoic by the PML [16] and source (Eq. (8)) boundary conditions respectively. The block structured mesh sketched in Fig. 3 consists of nine blocks with a total of 786 736 grid points. Four thousand points (0.5%) of host and overset grid are interpolated by Eq. (7) in total. The implementation of the PML and sponge layer boundary conditions produces an overhead of 12 690 points (1.6%) which is included in the total grid number. The typical spacing of 8×10^{-4} m for axial and radial direction is kept throughout the whole background mesh and theoretically allows to resolve frequencies up to 60 kHz. The fine resolution is mainly necessary to resolve the thin shear layers of the mean flow. There are only small variations from this mesh spacing in the overset grid. The resulting time step size is 5×10^{-7} s. Overall, 0.021 s of real time are calculated on a dual core

Table 1
Summary of the experimental set up.

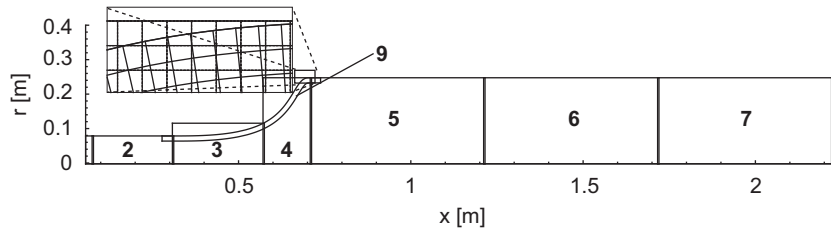|	Narrow inlet duct (IIC)	Wide inlet duct (IC)
Diameter [m]	0.157	0.494
Flow velocity [m/s]	104.582	11.064
Temperature [C]	12.427	17.639
Pressure [kPa]	93.443	99.527

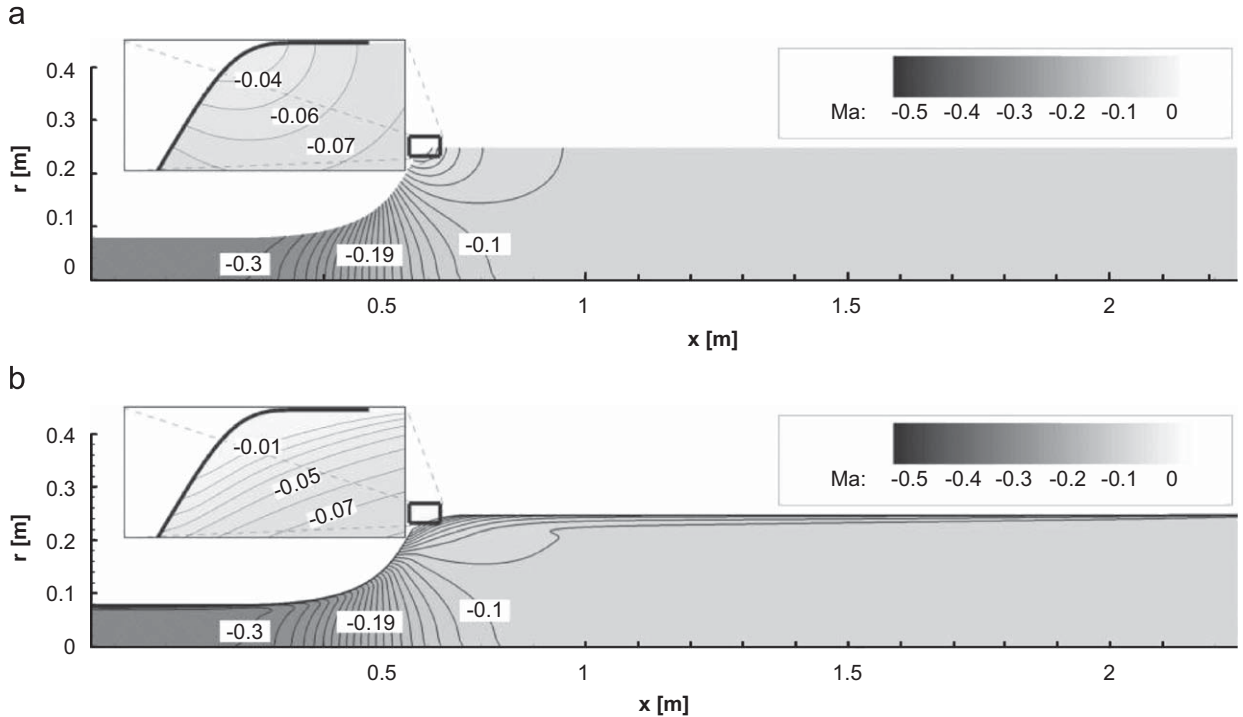**Fig. 3.** Meshing of the inlet duct by overset grids.

Fig. 4. Base flow Mach number distribution in the inlet duct. (a) Slip wall, isentropic model. (b) Shear layer, non-isentropic model.

Opteron machine with 2.2 GHz and four GB of main memory within 37 h for the isentropic model using MPI. The non-isentropic model requires the solution of an additional equation and therefore takes 39 h on the same system. The last 10 full periods (9.2×10^{-4} s) of the considered tone are included into the time average of the acoustic intensity.

To access the influence of two different mean flow assumptions, a slip wall condition is compared to a resolved shear layer defined by a Stokes boundary condition. The mean flow with wall bound shear layer was calculated using TRACE, a Navier–Stokes-solver for turbo-machinery applications developed by the German Aerospace Center [17]. For comparison, a mean flow based on a nonlinear Euler equation with a slip wall assumption is used. This mean flow is calculated on the structured mesh shown in Fig. 3 using the numerical method described in Section 2.2. However, a steady flow source is described at in and outflow and the model equations are replaced by an axisymmetric so-called PENNE approach [5], which has been implemented into the method for the simulation of nonlinear noise propagation [6]. The mean flow Mach number is shown in Fig. 4 for both, the slip wall and the shear layer at the wall. The major difference of the two base flow models is found in the solution in the region of the contraction (compare Fig. 4).

Two different mathematical model assumptions for the propagation of the acoustic perturbation following from Eq. (1c) and (1d) are compared using two different base flow conditions. The results for cases denoted by (A)–(D) are summarised in Table 2. The variety of cases is used to study a possible influence of the modelling on the acoustic solution. All four cases are presented and analysed in the following sections.

5. Results

The results and discussion are organised as follows. First in Section 5.1 the instantaneous sound field and the resulting wall sound pressure levels are presented. Then the sound field in the IC undergoes a modal analysis in Section 5.2. The

Table 2
The four model assumptions considered for comparison.

Notation	Mean flow	Energy equation
(A)	Euler potential flow shown in Fig. 4(a)	Full energy equation (1c)
(B)		Isentropic relation equation (1d)
(C)	Stokes boundary condition with shear layer shown in Fig. 4(b)	Full energy equation (1c)
(D)		Isentropic relation equation (1d)
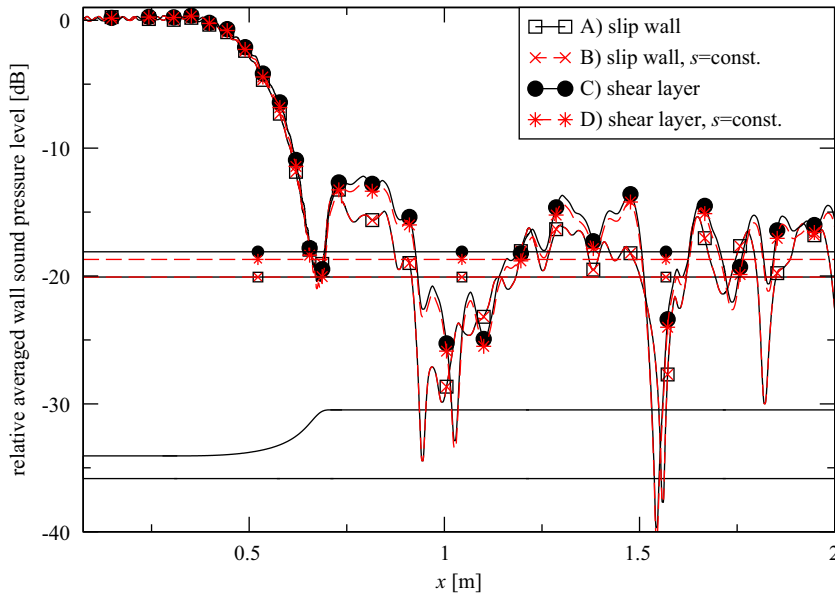
Fig. 5. Averaged sound pressure levels at the wall relative to the input level.

methods developed in Section 3 are employed in Section 5.3 to quantify the numerical error and in Section 5.5 to locate acoustic sources. Subsequently the grid convergence and the influence of the filter stencil are studied in Section 5.4. Finally, a model vision for the sound field is developed based on the time averaged acoustic intensity in Section 5.6.

5.1. Sound pressure level at the wall

First the sound pressure level at the wall is analysed. The numerical results are given in Fig. 5 for all four modelling assumptions presented in Table 2. The sound pressure level is normalised by a reference source level. This reference is taken from a wall point inside the sound source region in the IIC. The point represents the input of the source and is not affected by reflections. The duct is a wave guide. A change of the impedance in such wave guide, which is related to the duct area in the current example, in general produces reflections. Therefore, the inlet nozzle is supposed to be a source of reflections. However, the small variations of the wall sound pressure level in the IIC, found in Fig. 5, indicate that very small reflections towards the IC are present for all four cases.

The IC shows larger variations of the wall sound pressure level than the IIC. The average value of the wall sound pressure level in the IC is plotted as straight line in Fig. 5. The decrease of the sound pressure level between immediate inlet channel (IIC) and the upstream inlet channel (IC) is about 18 . . . 20 dB in average for all four modelling assumptions. Even though no detailed spatial data were provided, this is in a good qualitative agreement with the observed average wall SPL in the experiment.

When comparing the four modelling assumptions in Fig. 5, especially the axial location of the peaks and minima is found to be different, whereas the absolute range of variation and the average value are found to be similar. The variation of the physical model with the same mean flow produces hardly observable differences, when comparing (A) to (B). Slightly larger, but still very small variations are found in case of the shear layer boundary condition when comparing (C) to (D). Due to the different location of the peaks, the different mean flow profiles produce variations of up to 15 dB for local peaks when comparing (A) to (C) and (B) to (D). Nevertheless, the peak amplitudes are very similar and the average level in the IC differs by less than 2 dB.

The RMS value of the wall sound pressure in the IC ranges from 0.01% to 6% of the source value in the IIC for all four solutions. This corresponds to a relative wall sound pressure level attenuation in the range of -12 to $-40\,\mathrm{dB}$ from IIC to IC. Those observations underlined the participation of multiple radial modes at similar levels to the complex sound field of the inlet channel. Due to the different axial wavenumber of each radial mode of the $m = 13$ azimuthal mode, the relative phase of these modes changes with the axial location. In addition, as the origin of the modes is triggered by the inlet geometry and mean flow, the resulting superposition field at the wall depends only on the axial position. The observed sound pressure level is independent of the azimuth angle. Therefore, wall mounted microphones report equal sound pressure levels for all radial modes of the same azimuthal mode, independently of their azimuthal position. The instantaneous pressure contours for the example of case (C) are presented in Fig. 6 to underline the complex structure of the sound field in the IC.

A further analysis of the result is required to give details about the modal structure, which is the subject of the next section. Furthermore, based on Fig. 5 or 6, it is difficult to decide on the quality of the current numerical solution. As discussed the decreased wall sound pressure level could also be caused by numerical dissipation or interpolation errors due to the overset grid method. In particular the exact level of the all present numerical errors cannot be directly estimated with such a complex sound field of the inlet duct. The acoustic intensity is employed for this purpose in Section 5.3.

5.2. Modal analysis of the sound field in the inlet channel (IC)

The radial modes found in the IC are analysed by a modal analysis tool [18], to prove the presence of higher radial modes in the solution and quantify their contribution to the observed sound field. Fig. 7 shows the results of the radial mode analysis in the IC. The bars shown in Fig. 7 correspond to the sound pressure level of each single cut-on radial mode and the first cut-off mode ($n = 10$) of the $m = 13$ azimuthal mode relative to the input sound pressure level in the IIC. From Fig. 7 it can be seen that in general the $n = 4$ and 5 radial modes contribute at the highest level and all cut-on radial modes are present at a non-negligible amplitude in the IC.

The modal analysis results for the isentropic and non-isentropic model assumption, comparing the same flow conditions do not differ at all in case of the slip wall assumption, cases (A) and (B). Most of the radial mode amplitudes
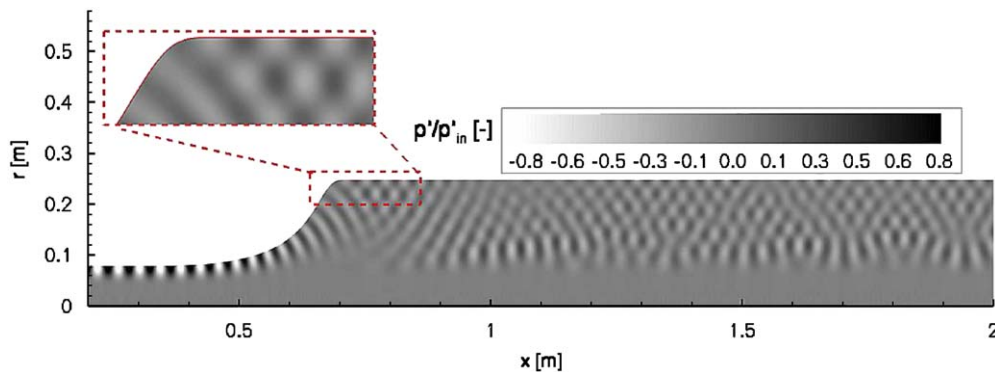

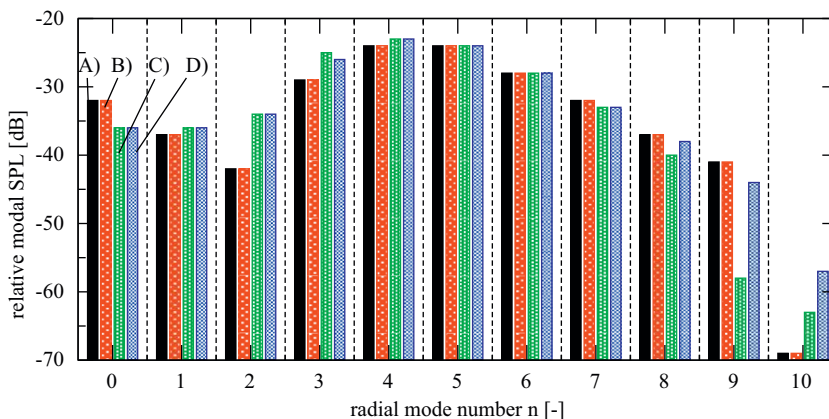**Fig. 6.** Instantaneous pressure contours (shear layer).

Fig. 7. Wall sound pressure level of each radial mode in the IC relative to the input in the IIC.

differ marginally by up to 1 dB in case of the realistic sheared flow conditions, cases (C) and (D), when varying the mathematical model. One exception is found for the $n = 9$ mode with shear layer assumption for the mean flow, which is found to produce a difference of 14 dB when comparing the two mathematical models (C) and (D). This is interesting on the background of the fact that the simplified isentropic model equations are not adequately chosen to describe the average flow field in case (D). The difference occurs only in one radial mode, but it shows that modelling simplifications like the application of a simplified isentropic pressure density relation may have a strong influence on the solution.

More significant differences of up to 17 dB are observed when comparing the different models for the base flow, the slip wall cases (A) and (B) to the boundary layer cases (C) and (D). The modal content is changed due to the presence of a shear layer. While the first three modes show a dynamic range of 9 dB with a clear preference of the $n = 0$ mode in case of a slip wall (A, B), the sheared base flow (C, D) balances the levels of these modes. In case of a wall bound base flow and a consistent non-isentropic modelling of it, the $n = 3$ mode is found to be increased.

Altogether, the results of the mode analysis reveal the strong scattering of energy into higher radial modes. This mode scattering in the inlet nozzle is geometry and mean flow induced and it prefers the radial modes around $n = 4$ and 5 in the given case. As higher modes carry more energy in the inner duct and less energy at the outer wall, the power level at the wall (compare Fig. 5) is decreased more than it would be expected due to the changing area. A modal analysis of the experimental result by Raitor et al. [3] is not available yet, such that a further validation of the current result with the experiment is not possible.

5.3. Acoustic power along the duct

Now, Eq. (14b) is considered to validate the acoustic solution. The average acoustic power flux $\langle P \rangle_t$ is plotted along the axis of the duct in Fig. 8. The values are normalised by the input power, which is here defined by the power flux in the IIC directly upstream the sponge layer of the sound source. This is necessary to avoid distortion of the input power by the artificial dissipation of outgoing waves inside the source layer. In consequence, the normalisation quantity is the resulting power flux of incoming and reflected waves in the IIC. In a potential mean flow without acoustic sources $\langle P \rangle_t$ should be equal to unity for all axial positions in the duct. The results indicate that this is not the case and acoustic sources, which include the effect of numerical dissipation and interpolation errors, are present. The acoustic power is approximately constant in the straight sections of IC and IIC for all four solutions, whereas in the nozzle section deviations up to 20% are observed. $\langle P \rangle_t$ first rapidly increases when entering the nozzle from the IIC. For all expect the shear layer case $\langle P \rangle_t$ decreases in the nozzle. Another jump is found at the end of the nozzle towards the IC, which equalises the level back to the value found in the whole IC. Strong oscillations are found in the region affected by the overset grid.

When considering the straight IC or the IIC section alone, the acoustic power remains approximately constant for all four cases. There is a small increase of $\langle P \rangle_t$ along the IC for the shear layer with full LEE model. When considering the conservation of the acoustic energy from IIC to IC, it is found that the overall acoustic power decreases by approximately 2–3% for all mean flow conditions expect for the shear layer with non-isentropic model (C), where the level increases by 15%. In this case the increase is considered to be a natural effect of the shear layer, which adds acoustic energy.
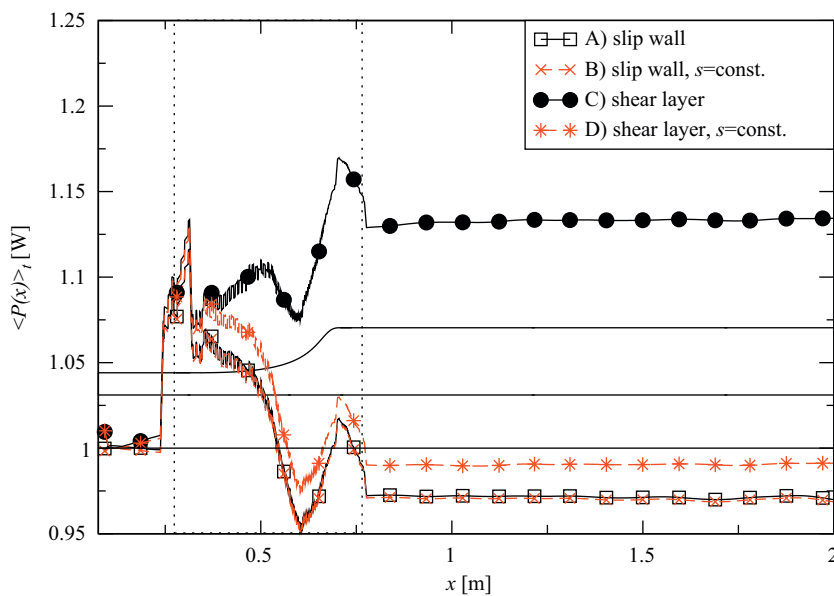

Fig. 8. Normalised acoustic power level $\langle P_a \rangle$ along the duct based on the intensity definition of Morfey [1].

A fourth-order interpolation is applied in the overset grid region. The numerical scheme is of fourth order as well. However, it is optimised in order to provide a better approximation of the wavenumber than a sixth-order scheme. Therefore, the order of accuracy for the overset grid may not be sufficient. The oscillations in the overset grid region point in the same direction. Resolution differences lead to grid oscillations. In all cases, the overall error from the overset grid region to the leading order determines the resulting error in the conservation of the acoustic energy. The numerical interpolation error as well as the physical sources due to the non-potential mean flow are localised in the region of the overset grid. Therefore, it is difficult to distinguish numerical and physical sources from the above observation. A more detailed view on the sources will be provided in Section 5.5 by the source power level.

The flow conditions calculated with the slip wall approximately meet the assumption of an irrotational, isentropic potential flow. As theoretically expected, isentropic and non-isentropic model equations do not show any difference for the cases (A) and (B). The two cases (C) and (D) with shear layer profile towards the wall are suspected to allow an exchange of energy between non-isentropic mean flow and acoustic waves. Thus the conservation of the acoustic energy would be disturbed by natural sources in the flow in cases (C) and (D). However, only in the case (C), where the shear layer is correctly modelled by a variant of the LEE, which allows non-isentropic mean flow conditions, the acoustic power increases by 15% (see Fig. 8). In case (D), which uses an isentropic mathematical model for the non-isentropic sheared base flow, the numerical errors and the physical source strength due to the mean flow seem to cancel. Therefore, the preservation of the acoustic energy is found to be best met for this case.

5.4. Further numerical experiments for the classification of the current result

The results indicate that the acoustic intensity is not fully conserved in the current example. However, the relative error is small. To further investigate the error level and assess the result, case (B) is picked.

The current mesh was originally designed to adequately resolve the third harmonic of the blade passing frequency with 9 points per wavelength (PPW). Thus, the resolution of the free-field wavelength against the flow at $Ma = 0.3$ is about 27 PPW at the BPF. The axial resolution of the first radial of the $m = 13$ mode in the IIC is found to be 47 PPW. As the resolution is much better than required, the grid convergence can be studied by reducing the order of the method to fourth order without optimisations. The mesh and overset grid are kept constant with this reduction. The resulting average acoustic power fluxes are shown in Fig. 9. As can be seen, the results do not differ. There is no measurable influence of the approximation order and the grid on the solution.

Furthermore, the parameters of the numerical filtering are varied in Fig. 9. First, the frequency of the filter application is kept constant and the filter coefficient σ_{filter} is increased from $\sigma_{filter} = 0.25$, which was used above, to $\sigma_{filter} = 0.75$. As can be seen from Fig. 9, the resulting acoustic power flux along the duct is similar between both cases. A slightly increased dissipation is observed for $\sigma_{filter} = 0.75$. While with the original setting less than 3% of the acoustic power are lost mainly in the overset grid section, the increased filtering coefficient adds a decay along the IC. Overall almost 5% of the acoustic energy are lost. The last test applies the selective artificial damping stencil of Tam et al. [10] as filter stencil. As can be seen from Fig. 10, this stencil has been optimised to obtain a larger pass band. However, the dissipation in the pass band is
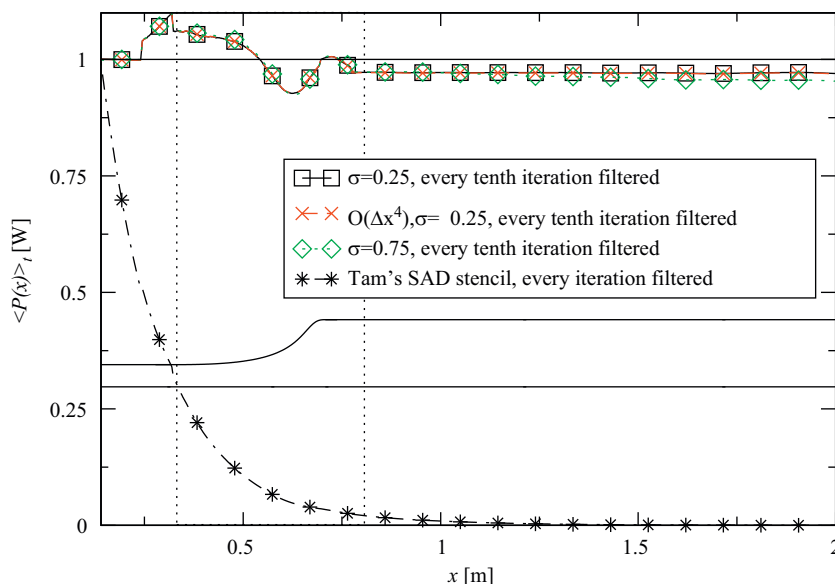

Fig. 9. Study of the grid convergence and influence of filtering coefficient and filtering stencil with case (B), shown in a spatially filtered power flux.
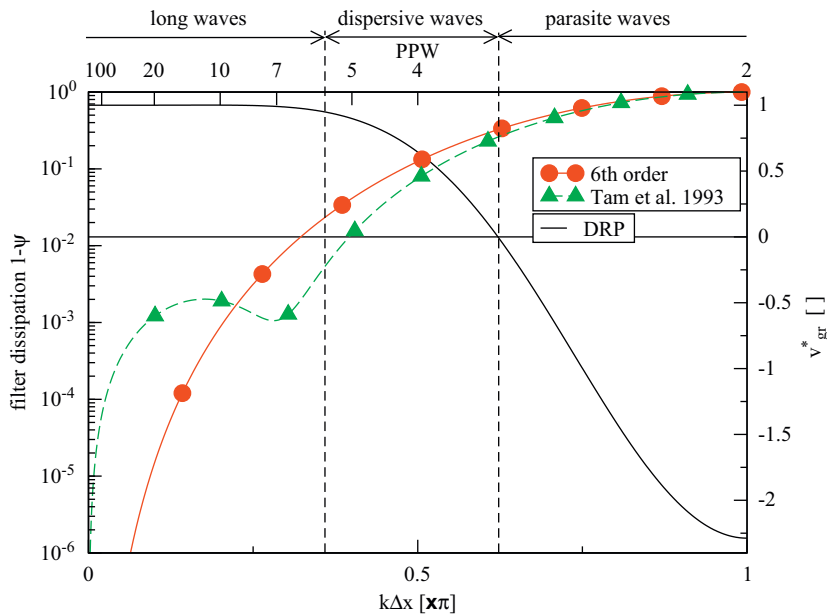
Fig. 10. Dissipation characteristics of the filter stencils and group velocity of the DRP scheme.

increased due to the optimisation. The acoustic power flux along the duct shows a strong decay when this filter is applied. More than 20 dB attenuation of the sound intensity level are observed.

To understand the result, the characteristics of the two different filtering stencils according to Eq. (4) are shown in Fig. 10. For comparison the group velocity of the DRP scheme and the related wavenumber ranges are given as found in Tam et al. [10]. The dissipation of the selective artificial damping (SAD) stencil is around 10^{-3} for a resolution of 50 PPW, whereas the dissipation of the non-optimised sixth-order filter is below 10^{-6}. The dissipation $1 - \Psi$ denotes the amplitude loss for one application of the filter. Due to the frequent application of the filter, the dissipation of the SAD stencil, which is applied as filter here, sums up and becomes intolerably large in the pass band. The Taylor filter on the other hand is able to keep control over grid oscillations with only small dissipation in the pass band.

5.5. Source location

In this section the source power level (QPL) defined by Eq. (13) is employed to find acoustic sources in the numerical solutions. The method is based on the identity of the average acoustic source strength with the divergence of the average acoustic intensity. The divergence in a cylindrical coordinate system is calculated based on the spatial derivatives obtained by using the DRP scheme. A negative QPL indicates a local annihilation of acoustic energy, whereas a positive value indicates a production of acoustic energy and an increasing acoustic power along the duct. The results are shown in Fig. 11. Only the two cases (B) "slip wall, s =const." and (C) "shear layer" are considered. In addition, the application of the very dissipative SAD-filter is considered. The scales are equalised between the figures. QPL values in the range of ± 100 dB are cut-off in order to focus on the dominant sources. In the cut out range of the QPL, sources of equal strength are located all over the duct. These sources are interpreted as numerical noise. Thus, the numerical noise level is assumed to be ± 100 dB for the QPL.

Almost no sources are found for case (B) shown in Fig. 11(a). The source for the decrease of the acoustic power, which was observed in Fig. 8 for the cases (A) and (B), is probably the interpolation error of the overset grid approach. This source of numerical error shows up as QPL activity along the boundaries of the overset grid block. Especially, the upstream end of the overset grid block ($x = 0.72$ m) shows a pattern of positive and negative sources. The results indicate that the fourth-order interpolation produces deviation from the conservation of acoustic energy in case (B). However, the small source regions only marginally raise from the background noise. At the up- and downstream end of the computational domain, the method identifies the sponge layer and PML zones as acoustic sources. These desired artificial sources are due to the modification of the governing equations in these regions. Furthermore, some sources are located at the wall in the IIC, which contribute to the oscillation of the overall acoustic power flux along x.

In contrast to the low source levels observed before for case (B), there is a large positive acoustic source along the outer wall of the nozzle for case (C) presented in Fig. 11(b). In this case the observed source levels clearly raise over the sources found all over the computational domain. The source region spans over the curved overset grid block as well as the background mesh. As in case (B) a pattern of positive and negative sources is found at the upstream end of the overset grid block ($x = 0.72$ m), which indicates the presence of interpolation errors in this region. However, the nozzle is clearly
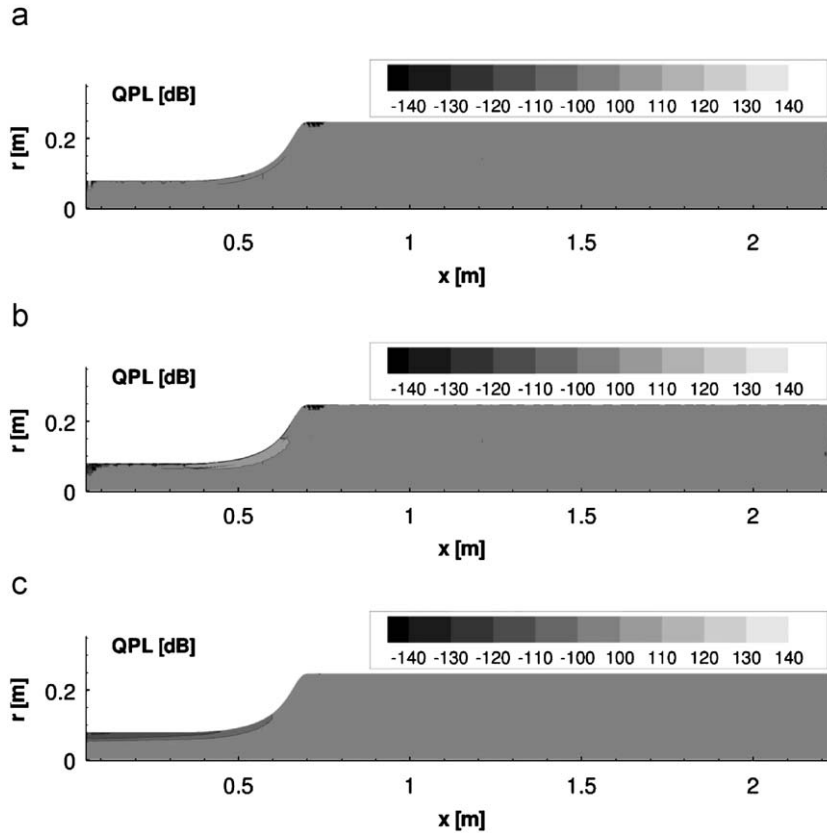
Fig. 11. Divergence of the time averaged acoustic intensity. An arbitrary value of $\langle P \rangle_t = 0.1$ mW is assumed as input level. (a) Slip wall, isentropic model (B). (b) Shear layer, non-isentropic model (C). (c) As (B), applying the SAD stencil as filter.

identified as source for the observed increase of the acoustic power. Therefore, the current result allows a further specification of the observations in the preceding section, where the integral value $\langle P \rangle_t$ increased by 15% between IC and IIC.

Finally, the SAD-filter presented in Fig. 11(c) shows the largest absolute QPL in this study. The large negative value corresponds to a strong attenuation of acoustic energy, which has been found in the acoustic power flux along the duct presented in Fig. 9 for this filter as well. The oscillations around ($x = 0.72$ m) are missing in this case, as the remaining power level of the acoustic waves in this region is below the threshold of the presentation. The same applies for the PML zone.

Altogether, the good quality of the numerical solution shown in the preceding section is underlined and the interpolation error of the overset mesh is quantified to be around 3% in total for the current result. Probably the application of a structured body-fitted mesh without overset grids would lead to a much larger error.

5.6. Tracking of the intensity path

In this section the acoustic intensity is employed to develop a simplified model vision about the complex modal acoustic field in the centrifugal compressor inlet duct. The averaged path of the acoustic energy through the inlet duct is visualised by power vectors. These power vectors are obtained by multiplying the acoustic intensity vectors by the area of an annulus on which the intensity is found in average and normalizing the result by an arbitrary input power. The results are plotted in Fig. 12. Concentrations of the acoustic power flux around $r = 0.1$ m are found at $x = 1$ and 1.6 m, which corresponds to the positions with the smallest amplitudes at the outer wall found in Fig. 5. In between the waves are reflected towards the outer wall of the duct. Thus, around $x = 1.3$ higher amplitudes are found at the wall in Figs. 5 and 12. The sound pressure level shown as contours in Fig. 12 underline the above findings.

As the acoustic wave length in the IC is small compared to the diameter, a ray model is also suitable to qualitatively describe the acoustic wave propagation in this section. The acoustic waves leave the opening inlet, heading towards the outer wall of the wider duct at an angle depending on their cut-off ratio. At the outer wall the waves get reflected towards the axis and are then reflected outward again, but at a lower angle as Fig. 12 shows. This finally produces points at the wall where the acoustic power is concentrated and points where only a small amount of energy is found as it was observed in
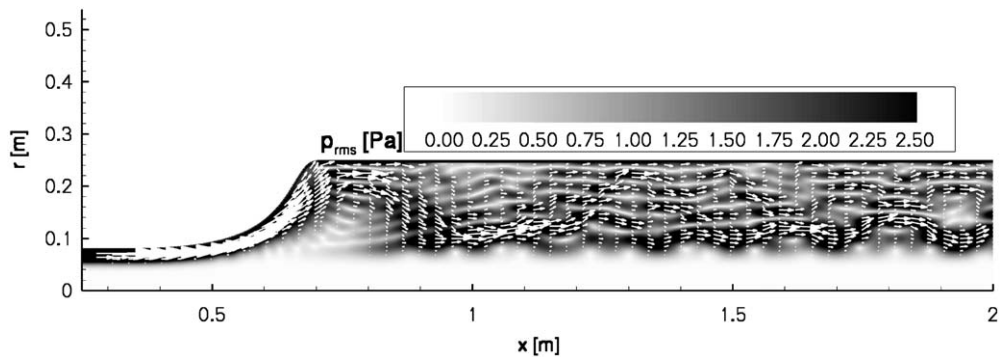
Fig. 12. Sound pressure level distribution and path of the average acoustic energy visualised by vectors **I**r for case (B).

Fig. 5. However, multiple rays, one for each mode, with different radiation angles are necessary to obtain the complex pattern. A single ray may, however, describe the close surrounding of the inlet nozzle up to the first reflection at the axis.

6. Conclusion

The detailed analysis and validation of a CAA result for a complex sound field has been presented by the example of a centrifugal compressor inlet duct. A modal axisymmetric CAA method is applied together with an overset grid approach to overcome the geometrical complexity of the problem, retaining a structured mesh.

The results are analysed for the acoustic energy conservation and a source location is provided. The acoustic intensity is used to assess the quality and accuracy of the numerical results, independently of an analytical solution. The source location by the acoustic intensity analysis provides a tool to understand the physical process of sound generation as well as to find numerical error sources. It is shown that the leading order error is introduced by the overset grid interpolation. However, it remains small within an engineering accuracy of 3% deviation from the conservation of the acoustic energy.

A mode analysis is applied. The modal content of the solution depends on the base flow assumption. However, independently of the base flow, the highest modal amplitude is found in the higher radial modes around $n = 4$ and 5. All other cut-on radial modes are present at a considerable level. The acoustic energy is not equally distributed over the duct area. Rather the transport of a majority of the acoustic energy takes place further away from the wall around $\frac{1}{3}$ of the duct radius, as an analysis of the intensity vectors shows. In consequence, the scattering into higher radial modes is identified as the reason for the reduction of the average sound pressure level at the wall by about 20 dB between inlet channel and immediate inlet channel.

The comparison of the different mean flow assumptions and model equations shows only small differences in the sound power level observed at the wall. However, with the acoustic intensity sound sources are found in the accelerating flow inside the inlet nozzle. The overall sound power level in the inlet duct is found to be increased by about 15% in case of realistic flow with shear layer at the walls modelled by the non-isentropic governing equations.

Further examples are given to demonstrate the strength of the intensity analysis. A very dissipative filter, which is obtained by using the selective artificial damping coefficients of Tam et al. [10] as filter stencil, is clearly identified as numerical error source by the overall average acoustic power flux in the duct as well as the source location by the acoustic intensity. The applied filter and the numerical method are found to have only small impact on the solution in the current example. This is probably a result of the high grid resolution in combination with the high quality of the grid, which could be achieved by applying an overset grid approach.

Altogether, various postprocessing methods for the analysis and assessment of numerical results based on the acoustic intensity and a modal analysis have been presented. The results demonstrate the versatile applicability of the time averaged acoustic intensity to understand and validate an aeroacoustic solution. This is a general result, with the potential to be transferred to all aeroacoustic applications in computational fluid dynamics. However, the adoption to radiation problems and problems involving hydrodynamic vorticity and entropy perturbations may require a further validation of the intensity definition and a method for extracting the acoustic velocity from the velocity perturbation.

References

[1] C. Morfey, Acoustic energy in non-uniform flows, *Journal of Sound Vibration* 14 (2) (1971) 159–170.

[3] T. Raitor, W. Neise, Sound generation in centrifugal compressors, *Journal of Sound and Vibration* 314 (3–5) (2008) 738–756.

[4] X. Li, C. Schemel, U. Michel, F. Thiele, Azimuthal sound mode propagation in axisymmetric flow ducts, *AIAA Journal* 42 (10) (2004) 2019–2027.

[5] L. Long, A nonconservative nonlinear flowfield splitting method for 3-D unsteady fluid dynamics, AIAA Paper 2000-1998, June 2000.

[6] C. Richter, L. Panek, F. Thiele, On the application of CAA-methods for the simulation of indirect combustion noise, AIAA Paper 2005-2919, May 2005.

[7] C.K.W. Tam, C. Webb, Dispersion-relation-preserving finite difference schemes for computational aeroacoustics, *Journal of Computational Physics* 107 (2) (1993) 262–281.

[8] F.Q. Hu, M.Y. Hussaini, J.L. Manthey, Low-dissipation and low-dispersion Runge–Kutta schemes for computational acoustics, *Journal of Computational Physics* 124 (1) (1996) 177–191.

[9] D. Stanescu, W. Habashi, 2N-storage low-dissipation and low-dispersion Runge–Kutta schemes for computational aeroacoustics, *Journal of Computational Physics* 143 (2) (1998) 674–681.

[10] C.K.W. Tam, C. Webb, T.Z. Dong, A study of short wave components in computational aeroacoustics, *Journal of Computational Acoustics* 1 (1993) 1–30.

[11] N. Schoenwald, L. Panek, C. Richter, F. Thiele, Investigation of sound radiation from a scarfed intake by CAA-FWH simulations using overset grids, AIAA Paper 2007-3524, May 2007.

[12] F. Hu, A stable perfectly matched layer for linearized Euler equations in unsplit physical variables, *Journal of Computational Physics* 173 (2) (2001) 455–480.

[13] C. Tam, Z. Dong, Wall boundary conditions for high-order finite difference schemes in computational aeroacoustics, *Theoretical and Computational Fluid Dynamics* 6 (6) (1994) 303–322.

[14] C. Richter, F. Thiele, X.D. Li, M. Zhuang, Comparison of time-domain impedance boundary conditions for lined duct flows, *AIAA Journal* 45 (6) (2007) 1333–1346.

[15] W. Eversman, Acoustic power in lined ducts, AIAA Paper 2004-2904, May 2004.

[16] F. Hu, On absorbing boundary conditions for linearized Euler equations by a perfectly matched layer, *Journal of Computational Physics* 129 (1996) 201–219.

[17] D. Nürnberger, F. Eulitz, S. Schmidt, A. Zachcial, Recent progress in the numerical simulation of unsteady viscous multistage turbomachinery flow, Isabe 2001-1081, Bangalore, September 2001.

[18] N.C. Ovenden, S.W. Rinestra, Mode matching strategies in slowly varying engine ducts, *AIAA Journal* 42 (9) (2004) 1832–1840.